Energy Engineering

Tech Science Press

DOI: 10.32604/EE.2021.014366

ARTICLE

Structure and Combustion Characteristics of Methane/Air Premixed Flame under the Action of Wall

Feiyang Li, Jianfeng Pan*, Chenxin Zhang, Evans K. Quaye and Xia Shao

School of Energy and Power Engineering, Jiangsu University, Zhenjiang, 212013, China

*Corresponding Author: Jianfeng Pan. Email: mike@ujs.edu.cn

Received: 21 September 2020 Accepted: 13 November 2020

ABSTRACT

In order to obtain the combustion characteristics of the CH_4/Air premixed flame under the action of the wall interaction, a study on the impact of the jet flame on the wall at different separation distances was carried out. The separation distance from the burner outlet to the lower surface of the wall is changed and the flame structure is obtained through experiments. The temperature, velocity and reaction rate are obtained through numerical simulation, and the law of flame characteristics change is obtained through analysis. The results show that as the separation distance increases, the premixing cone inside the flame gradually changes from a horn shape to a complete cone shape and the length of the premixing cone profile increases. Also, the peak temperature and velocity of the mixture in the axial direction gradually increase, and the temperature and velocity in the radial direction first increase and then decrease. The temperature gradient and velocity reach the maximum when the separation distance is 11 mm. The peaks of reactants (CH_4) net reaction rate intermediate products (CO) and products (CO_2, H_2O) on the axis and the axial distance corresponding to the peaks increase accordingly. The chemical reaction rate near the wall also gradually decreases with the increase of the separation distance.

KEYWORDS

Flame-wall interaction; separation distance; flame structure; air flow temperature; flow velocity; reaction rate

1 Introduction

Flame-wall interaction (FWI) is a two-way coupling process between the flame and the solid wall. In most practical applications, such as internal combustion engines and gas turbines, combustion occurs in closed containers. Quantitative measurements of FWI processes in practical combustion systems, such as engines, are very challenging because of the limited access available for optical diagnostic methods, small length scales in boundary layers due to elevated pressures, and less controlled or even unknown inflow and boundary conditions. To overcome these restrictions, generic experiments were developed to benchmark the relevant physical and chemical properties of FWI at laboratory scale [1]. Typical working conditions are adiabatic flame temperatures up to 2500 K and wall temperatures below 1000 K. The wall will cause the flame to be greatly affected by gas dynamics, thermodynamics and reaction kinetics, and easily cause heat loss and wall quenching, resulting in incomplete combustion and increased hydrocarbon emissions, such as CO [2,3]. Meanwhile, the local thermal stress on the wall under the action of heat flow will cause the wall material to fatigue and fail, reducing the reliability of the burner [4].

The development of modern combustion devices is toward higher power density: in this case, flame-wall interaction becomes more important. Therefore, a comprehensive understanding of the flame-wall interaction is of great significance for the design of combustion chambers of internal combustion engines, gas turbines and rocket engines [5–9].

The jet flame impacting the wall model is a typical flame-wall interaction model, which is widely used in industrial heating and melting, material processing, safety research and aerospace [10–13]. Owston et al. [14] observed higher heat release rate (HRR) at the wall during quenching. This was attributed to the low temperature chemistry which becomes dominant at the cold wall. Hindasageri et al. [15] applied inverse heat conduction (IHCP) technology to obtain the heat flux distribution of the methane/air premixed flame impinging on a flat plate. The height of the dimensionless flame premix cone alone determines the Nusselt number and effectiveness. Ray et al. [16] studied the heat transfer characteristics of a laminar methane/air flame impinging on a cylindrical surface. The results show that, compared with the flat plate, a higher heat flux can be generated on the surface of a cylinder in the stagnation zone, while it is opposite in the wall jet region. Jarray et al. [17] used computational fluid dynamics to simulate the heat transfer process of the methane-air premixed flame impinging on the composite plate, and found that the increase in Reynolds number promotes the total heat transfer between the plate and the flame. Tuttle et al. [18,19] studied the flame structure and stability when a methane/air premixed flame hits the wall. The heat flux sensor, calorimeter and reverse heat transfer technology are used to directly measure the heat flux of the flame on the target plate. Dabireau et al. [20] analyzed different types of hydrogen/oxygen flame-wall interactions. The results show that the wall heat flux caused by the premixed flame just before quenching is higher than that of the diffusion flame.

The flame-wall interaction is currently one of the main mechanisms of unburned hydrocarbon emissions. It is important to study the heat transfer characteristics under the action of the wall and the chemical reactions near the wall to improve combustion efficiency and suppress pollutant emissions [21–23]. Dong et al. [24] conducted an experimental study on the FWI characteristics of an anti-diffusion jet flame (IDF) when it hits the wall. The effects of the distance between the dimensionless nozzle and the wall (H/da) and the jet outlet diameter (da) on the static pressure of the wall and the heat flux in the wall impact area were compared. The results show that when the maximum stagnation pressure on the wall is a bell-shaped curve, the distribution curve of the heat flux presents different shapes under different H/da. Zhen et al. [25] studied the CO and NO_x pollutants produced when swirling and non-swirling inverse diffusion flames (IDF) hit the wall. The results show that, due to more air entrainment around, the concentration of CO and NOx after the swirling flame hits the wall is lower than the corresponding pollutant concentration in the non-swirl flame. Dalvi et al. [26] compared the heat transfer characteristics of the isothermal gas jets and the reacting flame jets. It revealed that the rate of heat transfer from the flame jet to a targeted solid surface depends on the structure of the flame, convective and radiative properties of the constituent gas species of the flame and the temperature of the gas within the boundary layer in vicinity of the plate. The current research on the flame-wall interaction mostly focuses on the effect of flame on the wall, while the research of the flame on the wall is relatively few. And the research on the change of heat transfer characteristics and the chemical reaction near the wall is not enough.

This paper mainly discusses the influence of different separation distance on the combustion characteristics of CH_4/air premixed flame. Taking the distance from the burner exit to the lower surface of the wall as the separation distance of the wall, the changes in the flame structure of the CH_4/Air premixed jet at different separation distances are studied through experiments. Furthermore, the effects of different separation distances on the temperature, velocity and reaction rate of the airflow are studied by numerical simulation.

2 Experimental and Numerical Simulation Methods

2.1 Experimental Device and Method

Fig. 1 is a schematic diagram of the experimental setup for premixed jet flame wall interaction. Fig. 2 is a schematic diagram of the flame wall interaction.

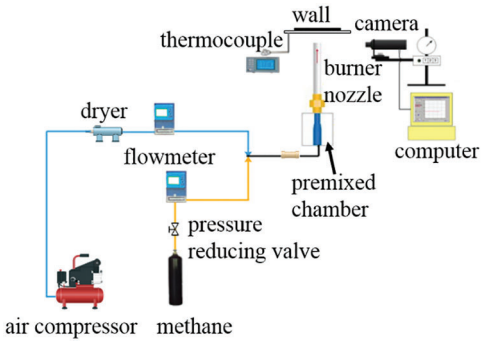

Figure 1: Schematic diagram of experimental setup

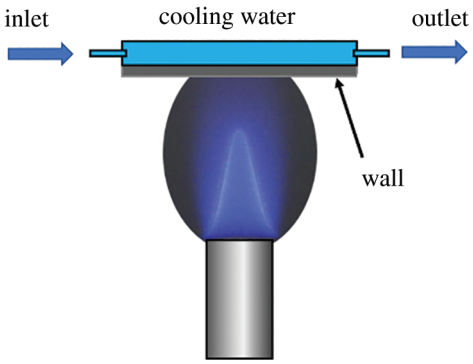

Figure 2: Schematic diagram of flame-wall interaction

Methane (purity of 99.99%) and air flow out of the gas tank and air compressor respectively. The output pressure and equivalence ratio are controlled by the pressure reducing valve and the mass flow meter respectively. The model of the mass flow meter is DSN-MFC 600 CD, the measurement accuracy is ±1%, and the response time is less than 1s. The methane and air enter the premixing chamber through the three-way pipe and are fully mixed. A tempering valve is fixed in front of the premixing combustion chamber to prevent backfire. The premixed gas is ignited at the outlet of the circular tube jet burner. The material of the round tube burner is 304 stainless steel, its inner diameter is 6 mm, and the wall thickness is 0.5 mm. Sodium silicate high temperature glue is used for adhesion and sealing between the burner and the base. The circular tube jet flame impinges on a square 304 stainless steel wall with a thickness of 3 mm and a length and width of 100 mm. A water cooling device is installed above the wall to keep the wall temperature at 299 K–305 K, and the height of the wall is controlled by an adjustable bracket. A K-type thermocouple is fixed at the inlet and outlet of the water cooling device to measure the temperature of the inlet and outlet.

A thermocouple is used to measure the temperature on the center line of the lower surface of the wall. The wall is symmetrical about the axis. Therefore, 9 points are distributed on each side of the wall and placed at an interval of 2 mm. The temperature of each thermocouple is measured five times, and the average

temperature is taken to reduce the influence of voltage output fluctuation. The diameter of the K-type thermocouple is 0.5 mm, the measurement temperature range is –40°C~400°C, and the measurement error is ±0.3%. A camera is used to record the flame shape and flame length, and a CH filter is installed in front of the camera lens to capture the CH distribution of the flame. The camera model is PENTAX K-50, and the effective pixels are 16.28 million. During shooting, the aperture value is set at F5.6 and the sensitivity is set at ISO1600. The center wavelength of the CH filter is 430 nm, the bandwidth is 30 nm, and the cut-off depth is od2-od3. In the post-processing step, the center of the jet burner outlet end face is taken as the reference point, and the position of the tip of the premixed cone in the picture is read and recorded. The position with the most frequent occurrence in multiple photos is the effective value, and the effective value is recorded as the height value of the premixed cone.

The coordinate system in the experiment is defined as follows: take the center point (stagnation point) of the lower surface of the wall as the origin; Z is the axial distance on the symmetrical axis from the stagnation point to the burner outlet; R is the radial distance, and the direction points to the edge of the wall along the stagnation point. The flame starts from the outlet from bottom to top, forming two layers of flame. The inner layer is a rich premixed flame, which is a luminous area with strong chemical reaction, called the premixed cone. When the CO and H_2 produced by combustion meet the surrounding air, a diffusion flame is formed in the outer layer of the premixed cone, which is called the diffusion cone. The height of the premixing cone is L_f, the vertical distance from the stagnation point of the wall to the apex of the premixing cone is δ_f, the inner diameter of the burner is D, and the vertical distance from the plane where the jet burner exits to the lower surface of the stainless steel wall is H (referred to as separation distance), as shown in Fig. 3.

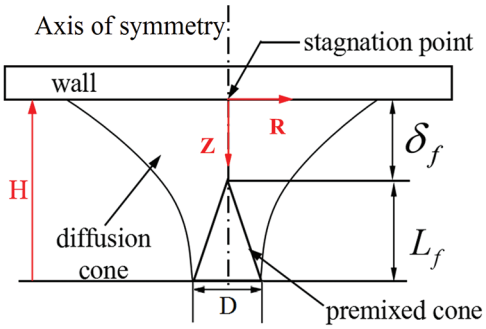

Figure 3: Schematic diagram of jet flame impacting metal wall

2.2 Numerical Simulation Method

In order to further study the influence of the wall on the premixed flame structure and combustion characteristics, a two-dimensional numerical calculation model of the methane/air premixed combustion process under the action of the wall was established, as shown in Fig. 4. The geometric model is symmetric about the wall axis. In order to reduce the computational cost, 1/2 of the model is selected for simulation.

To ensure that the grid division has no effect on the solution result, the grid independence verification is carried out before the numerical calculation. A structured grid and equivalence ratio of 1.0, Reynolds number of 550, separation distance of H = 3D (H = 18 mm), and axis temperature are used for the grid independence study. For this model, local mesh refinement is performed in the jet flame region (0 mm ≤ y ≤ 4 mm; 0 mm ≤ x ≤ 18 mm) and near the wall (17 mm ≤ x ≤ 18 mm), as shown in Fig. 5. Using the GAMBIT software, the model is divided into four different grid densities: 14756, 23086, 44911, 100889. Among them, when the number of grids is 44911, the temperature profile is the closest to 100889, and the result of the grid number of 14756 is quite different from other results, as shown in

Fig. 6. Therefore, considering the accuracy and the efficiency of the numerical calculation, the model with grid number of 44911 is used to carry out the rest of the simulations in this research.

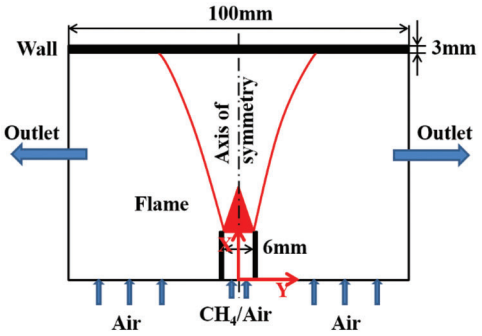

Figure 4: Physical structures of jet flame and wall interaction

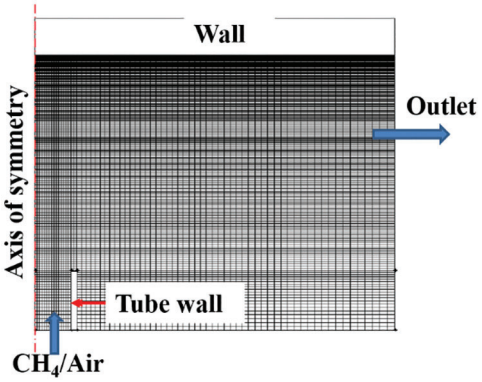

Figure 5: Mesh distribution corresponding to the model at D = 6 mm and H = 3D

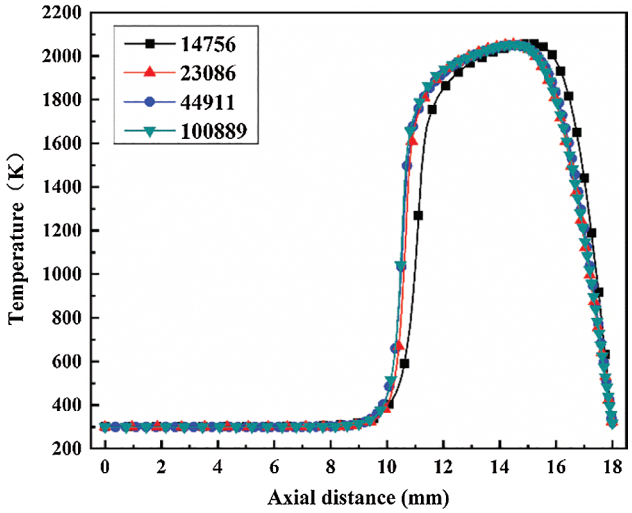

Figure 6: Temperature distribution on the axis of symmetry (D = 6 mm, H = 3D, Φ = 1.0, Re = 550)

The fluent software is used for the simulation. The laminar finite rate model, Reynolds number of 550, methane/air premixed gas, equivalence ratio of 1 and 0.1 MPa atmospheric pressure are selected for the simulation. The boundary condition of the jet inlet is set as velocity inlet and the inlet temperature is set as 300 K. Moreover, the outlet boundary condition is set as pressure outlet, and the water wall temperature is set at 300 K. The SIMPLE solving algorithm was chosen for the pressure - velocity coupling. This paper uses the methane/air gas phase reaction mechanism proposed by Titova et al. [27] in the numerical simulation calculations. The mechanism includes 26 gas components and 108 reversible elementary reactions.

The reaction process of methane and air premixed flame combustion and the gas flow should follow the laws of conservation of energy, conservation of mass, and conservation of momentum [28].

The definition of equivalence ratio in this paper is as follows:

$$\phi = \frac{(A/F)_{stoic}}{(A/F)_{actual}} \tag{1}$$

where $(A/F)_{stoic}$ is the chemical equivalent air-fuel ratio and $(A/F)_{actual}$ is the actual air-fuel ratio.

The Reynolds number of methane/air mixture jet outlet is defined as follows [29]:

$$\mathrm{Re} = \frac{v_{exit}\, D\rho_{mix}}{\mu_{mix}} \tag{2}$$

$$\rho_{mix} = \sum_i \rho_i Y_i \tag{3}$$

$$\mu_{mix} = \frac{\sum_i \mu_i X_i \sqrt{M_i}}{\sum_i X_i \sqrt{M_i}} \tag{4}$$

where, v_{exit} is the velocity of the mixture at the burner outlet, D is the inner diameter of the burner, ρ_{mix} is the density of the mixture, μ_{mix} is the dynamic viscosity of the mixture, Y is the mass fraction, X is the mole fraction, and M is the relative molecular mass.

2.3 Experimental Verification of the Model

In order to verify the accuracy of the simulation model, the numerical simulation results are compared with the experimental results. Three separation distances (H = 6 mm, 11 mm, 18 mm) were selected for experimental verification. Among them, H = 6 mm, 11 mm and 18 mm correspond to three cases of L_f (premixed cone height) < H (separation distance), L_f = H and L_f > H, respectively. Fig. 7 shows the temperature distribution on the center line of the lower surface of the wall. Under the three separation distances, the experimental and simulated values in the area near the center of the wall (when the radial distance is less than 5 mm) are almost consistent. However, far away from the center (when the radial distance is greater than 10 mm), the simulated temperature begins to be higher than the experimental temperature. The maximum errors for H = 6 mm, 11 mm and 18 mm are 2.33%, 3.03% and 2.24%, respectively, which indicates that the simulated curves are in good agreement with the experimental ones. The reason for the lower temperature measured far away from the stagnation point of the wall in the experiment is that the wall is far away from the flame, which absorbs less heat and dissipates more heat. Especially at the edge of the wall, the heat dissipation area increases and the heat dissipation effect of air on the wall is enhanced, which is not considered in the simulation.

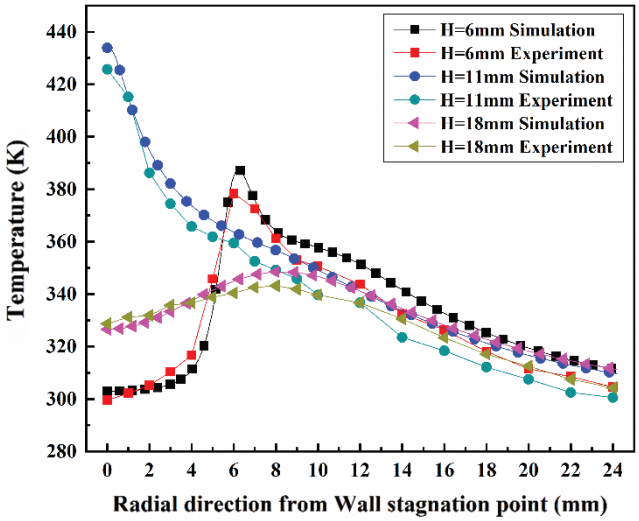

Figure 7: Comparison of temperature distribution on the center line of the lower surface of the wall with different separation distance H (Φ = 1.0, Re = 550)

In order to further verify the accuracy of the simulation results, the distribution of CH radical [30] is compared, as shown in Fig. 8. In order to clearly differentiate the circular tube combustion chamber from the flame, the outline of the combustion chamber is drawn with a black wire frame. It can be seen from the experimental pictures that when the separation distance h is 18 mm, the distribution of CH presents a conical structure with a length of 10.8 mm. The position of CH tip obtained in the simulation is 11 mm, with an error of 1.85% from the experimental value, and the shape is also conical. Therefore, in combining the error in the temperature distribution on the center line of the lower surface of the wall, the calculation model used can be considered reliable.

3 Results and Discussion

3.1 The Transformation of Flame Shape at Different Separation Distances

In analyzing the effect of different separation distances on the flame shape, the equivalent ratio is maintained at 1.0 and the Reynolds number is 550. Fig. 9a shows the flame shape at different separation distances. In the experiment, H values of 6 mm, 9 mm, 11 mm, 15 mm, 18 mm and 24 mm are selected as the six positions of the wall gradually away from the burner outlet, including the wall under the premixed cone tip ($H < L_f$), the wall near the premixed cone tip ($H \approx L_f$) and the wall gradually away from the premixed cone ($H > L_f$).

It can be seen from Fig. 9a that as the separation distance increases, the premixed cone and diffusion cone gradually turn to a complete shape from trumpet shape [31]. In the locally enlarged flame picture, the dashed white line represents the outer diffusion cone of the flame, and the red outline represents the premixing cone inside the flame. When the separation distance is 6 mm, the separation distance is much smaller than the complete premixing cone height ($H < L_f$) under this working condition, causing the flame to be "cut off" by the wall. The unburned combustion premixed gas directly impacts the wall flame, causing the flame to extend radially along the wall, forming a circular flame parallel to the wall. A cooling center core is produced in the central area [32], which weakens the degree of flame burning in the central area of the wall. When the separation distance is increased to 9 mm, the cooling center core range is reduced. When the separation distance is 11 mm, the cooling center core disappears, which is the critical point for the premixing cone to transform from a trumpet shape to a complete cone shape. The separation distance is approximately equal to the height of the premix cone ($H \approx L_f$), and the tip of

the premix cone is closest to the center point of the lower surface of the wall. When the separation distance increases from 11 mm to 24 mm, the trumpet shaped diffusion cone gradually shrinks and approaches the complete shape, as shown by the white dotted line. As the separation distance gradually increases, the color of the diffusion flame gradually becomes lighter. The reason is that after the separation distance increases, the wall is farther from the flame, and the amount of ambient air entrained into the combustion zone increases. When the CO and H_2 produced by the combustion encounter a large amount of surrounding air, the concentration is diluted and the intensity of combustion is weakened, resulting in a lighter color of the diffusion cone. Fig. 9b shows the distribution of CH at different separation distances. When the separation distance is small, due to the effect of the wall, the heat loss generated by the flame increases and the amount of air entrained into the combustion zone is less, and the flame burns insufficiently, resulting in the formation of more CH and C_2 free radicals [29]. When the separation distance is 6 mm, the outline of CH is the brightest, especially near the wall, indicating that more CH radicals are formed here.

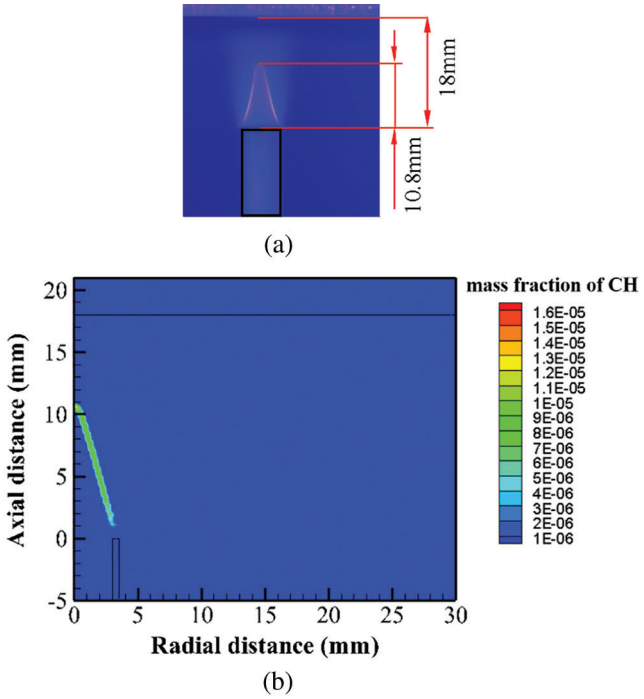

Figure 8: Comparison of CH concentration distribution zone in the experimental data and numerical data (a) Experimental shooting of CH pictures (b) The distribution of CH mass score obtained by simulation

It can be seen from Fig. 9 that as the separation distance increases, the height of the premix cone also increases. Especially when the separation distance increases from 6 mm to 11 mm, the increase is larger. Fig. 10 is an increase curve of the height of the premix cone when the separation distance increases from 11 mm to 24 mm. The height of the premix cone increases from 10.5 mm to 11 mm, and the increase is gradually flat. The reason is that when the separation distance is low (6 mm < H < 11 mm), the premixed cone will deform seriously under the action of the wall. When the separation distance is large (11 mm < H < 24 mm), the influence of the wall surface on the length of the premixed cone is small, and the premixed cone can always keep a complete cone.

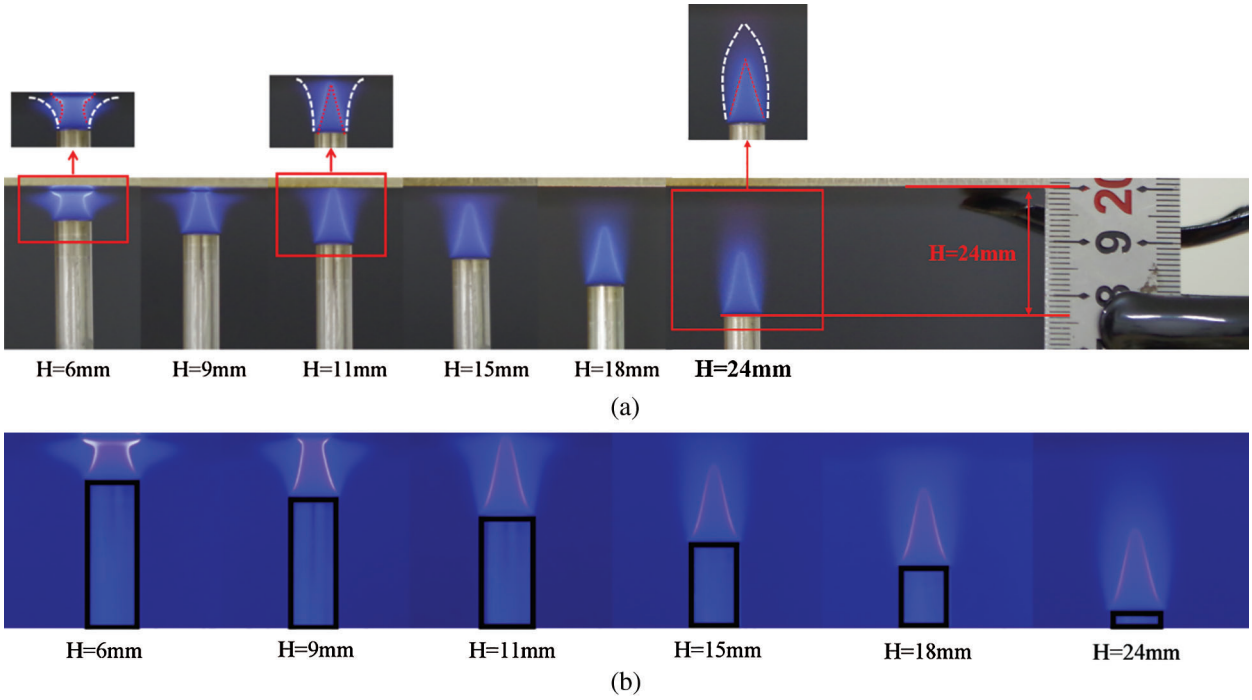

Figure 9: Flame shape and CH distribution at different separation distances (a) Flame shape under different separation distances (b) CH distribution under different separation distances

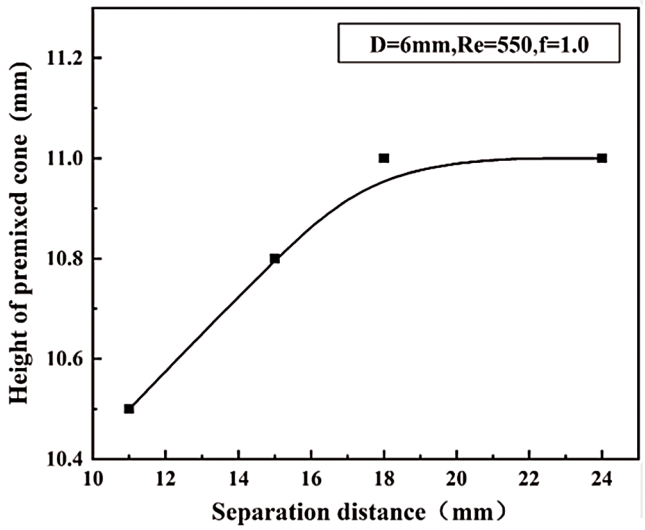

Figure 10: Length of premixed cone at different separation distances

3.2 Gas Temperature and Flow Velocity at Different Separation Distances

In this section, the temperature and velocity distribution along the axis and the radial direction with Z = 0.05 mm near the wall are simulated when the equivalence ratio is 1.0, the Reynolds number is 550, and the separation distance h is 6 mm, 9 mm, 11 mm, 15 mm, 18 mm and 24 mm. In order to more intuitively show the temperature distribution in the axial and radial directions under the action of the

wall, the isothermal distribution cloud map when the tip of the premixing cone is closest to the wall at H = 11 mm is selected, as shown in Fig. 11.

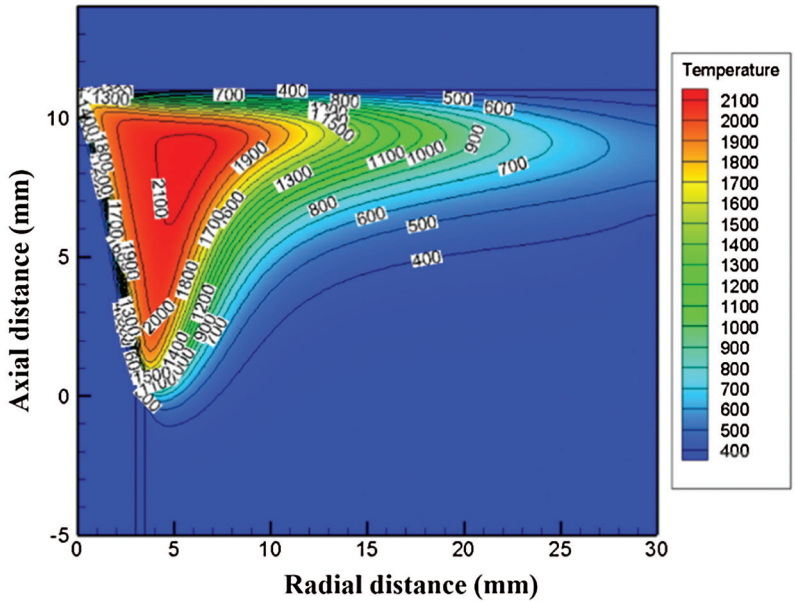

Figure 11: Isothermal distribution cloud map with separation distance H = 11 mm

Fig. 12 shows the temperature and velocity distribution profiles on the symmetry axis at different separation distances. Figs. 12a and 12b are the cases where the separation distance H is 6 mm and 9 mm respectively, the speed and temperature peaks on the symmetry axis are the smallest. As the axial distance increases, the speed on the symmetry axis decreases monotonously and drops to 0 m/s at the wall. The temperature on the symmetry axis is maintained at 300 K as the axial distance increases, which is the same as the temperature of the unburned mixture. This is because the separation distance is less than the height of the premix cone, and the temperature on the symmetry axis is the temperature of the unburned mixture [33–36]. When the separation distance H increases to 11 mm, as shown in Fig. 12c, the cooling center core disappears, and the premixing cone presents a complete cone. The peaks of temperature and velocity on the symmetry axis all appear near 10.58 mm in the axial distance, and then rapidly decrease. Unlike the temperature curve, the velocity curve drops slightly before reaching the premixing cone. This is because the wall surface is close to the tip of the premixing cone, which has a greater impact on the mixture. Under the action of the wall, the pressure near the premixed cone tip increases, and the increase of pressure will lead to the decrease of kinetic energy. Therefore, the velocity value of the mixed gas on the symmetry axis decreases slightly below the tip of the premix cone. Due to the violent chemical reaction in the premixing cone area, the temperature rise reaches its peak. The peak velocity is due to the high temperature of the combustion products in this area, which causes the density to decrease and the axial velocity to increase [33]. When the separation distance is further increased to 15 mm and 18 mm, as shown in Figs. 12d and 12e, the changes in these two cases are similar. Although the wall surface is far away from the tip of the premix cone when the separation distance is 15 mm and 18 mm, the peak temperature of the mixed gas on the symmetry axis is higher than the corresponding temperature peak when the separation distance is 11 mm. This is because when the distance between the premixed cone tip and the wall is small [37], the heat loss increases, which leads to a decrease in temperature. Moreover, because the wall is far away from the premixed cone, the space for secondary

reaction in the outer diffusion zone is increased. The heat released by the reaction leads to the temperature on the center line increasing sharply. Fig. 13 also fully illustrates that when the tip of the premixing cone is closer to the wall, the greater the contact area, the greater the wall heat loss. When the separation distance is 6 mm, the contact area between the flame and the wall is the largest, and the wall heat loss is also greater. As the separation distance increases, the contact area of the flame on the wall becomes smaller and the distance becomes larger, resulting in less and less heat loss on the wall. When the separation distance increases to 24 mm, the velocity on the symmetry axis reaches the peak at the axial distance of 11 mm and then decreases rapidly. There is a small secondary increase in the axial distance of 13 mm to 16 mm. This is because the wall is far away from the tip of the premixed cone. After passing through the internal reaction zone, there is still enough space between the combustion products and the wall surface and the flow velocity can be developed again, resulting in secondary acceleration.

Fig. 14 shows the temperature and velocity distribution in the radial direction near the wall (Z = 0.05 mm) at the six separation distances above. It can be seen from the figure that as the separation distance increases; both the peak temperature and velocity both increase first and then decrease. When the separation distance is 11 mm, the maximum temperature peak is 585 K, which occurs at a radial distance of 0 mm. At this time, the distance between the wall and the tip of the premix cone is the closest, so the temperature peak near the wall is the largest. When the separation distance h is less than 11 mm (H = 6 mm and 9 mm), the flame cannot fully extend due to the small separation distance. A cooling center core is formed at the center of the wall, and the mixture directly impacts the wall without reaction, resulting in lower temperature near the wall. As the separation distance increases, the cooling center core gradually decreases and the temperature gradually increases. The peak value of the temperature gradually approaches the center point of the wall. When the separation distance H is greater than 11 mm, the temperature peak value decreases as the separation distance increases. This is because after the wall gradually moves away from the premix cone, only the high-temperature mixed gas after combustion touches the wall (especially when the wall is far away (H = 18 mm and 24 mm)), the mixed gas is diluted and cooled by the ambient air. As a result, the temperature peak near the wall gradually decreases. In addition, when the separation distance H is 18 mm and 24 mm, the corresponding temperature peaks are 383.5 K and 375.2 K, respectively. In both cases, the temperature peak occurs far away from the stagnation point. The reason is that the mixed gas has accelerated flow in the jet area near the wall (5 mm < radial distance < 12 mm), as shown in Fig. 14b. When the separation distance H > 10 mm, the temperature near the wall first increases and then decreases. With the increase of the radial distance, the velocity near the wall will change at a certain radial distance. The change of velocity strongly affects the heat transfer of the wall and thus the temperature near the wall [33]. In the figure, when the separation distance is 18 mm and 24 mm, the speed gradually increases in the range of 5 mm to 12 mm in the radial distance, and finally rises to the peak at a radial distance of 12 mm.

3.3 Reaction Rates of Key Components at Different Separation Distances

This section compares the reaction rates of key components on the symmetry axis based on the six different separation distances above. From the reactants, intermediate products to products, a detailed analysis is carried out to understand the $CH_4 \rightarrow CO \rightarrow CO_2$ transformation process.

Fig. 13 shows the change in the CH_4 net reaction rate on the symmetry axis under different separation distances. The net reaction rate refers to the difference between the generated reaction rate and the consumed reaction rate under the same gas phase composition. It can be seen from the figure that when the separation distance is low (H = 6 mm and 9 mm), the net reaction rate of CH_4 on the symmetry axis is always maintained at 0. It shows that there is no chemical reaction of the mixture in the axial direction, and the reactants are not consumed. Because the height of the tip of the premixing cone at this time is greater than the height of the wall surface, the premixed fuel does not chemically react in the axial direction, but directly impacts the wall

surface, forming a cooling center core on the wall surface. At this time, the wall temperature on the axis is the same as the temperature of the premixed fuel, as shown in Figs. 12a and 12b. When the separation distance increased to 11 mm, the net reaction rate at the axial distance of 10.45 mm decreased rapidly to the maximum value of 42.56 kg/m^3/s. This indicates that a violent chemical reaction has taken place here, and methane is consumed rapidly. When the separation distance is 11mm, the tip of the premix cone is closest to the wall at this time, and the tip of the flame is the area where a strong chemical reaction occurs. The axial distance of 10.45 mm is where the tip of the premixing cone is located. At this time, CH_4 reacts violently with oxygen, and the temperature suddenly rises, as shown in Fig. 12c. CH_4 is quickly consumed, so the net reaction rate of CH_4 is reduced to a maximum. When the separation distance increased from 11 mm to 24 mm, the distribution of methane net reaction rate curve was similar to that of H = 11 mm. However, when the separation distances were 15 mm, 18 mm and 24 mm, the maximum net reaction rates occurred at the axial distances of 10.59 mm, 10.71 mm and 10.73 mm, respectively. Because the axial distance at which the maximum rate occurs at this time corresponds to the height of the premixing cone of the flame, the change of the premixing cone height when the separation distance is 15 mm, 18 mm, and 24 mm is shown in Fig. 10. In addition, when the separation distance is 11 mm, the maximum net consumption rate of CH_4 is the smallest, which indicates that the methane involved in the reaction at the tip of the premixing cone is reduced. Because the tip of the premix cone is closest to the wall at this time, the heat loss increases, the combustion intensity decreases, and the reaction rate decreases as well. When the separation distance increases from 11 mm to 24 mm, the heat loss on the water wall reduces and the maximum net CH_4 consumption rate increases as the distance between the premix cone tip and the wall. When the separation distance increases from 11 mm to 24 mm, the distance between the tip of the premixing cone and the wall surface gradually increases, and the wall heat loss gradually decreases, as shown in Fig. 13. Moreover, there is a gradual increase in the axial temperature, as shown in Figs. 12c, 12d and 12e.

Fig. 16 shows the profile of net CO reaction rate along the symmetry axis under different separation distances. The net reaction rate of CH_4, corresponding to the net reaction rate of CO is 0 kg/m^3/s when the separation distance is small (H = 6 mm and 9 mm). Because the height of the tip of the premix cone is greater than the height of the wall surface at this time, in the axial direction, the premixed fuel directly impacts the wall surface and no chemical reaction occurs, so there is no CO emission. When the separation distance is greater than the height of premixed cone, the maximum net formation rate (positive value) and maximum net consumption rate (negative value) appear in the net reaction rate of CO. The peak value of the maximum net CO production rate and the peak value of CH_4 consumption in Fig. 15 are almost the same. However, before the end of CH_4 combustion, the maximum net consumption rate of CO reaches the maximum value, which indicates that the generated CO begins to be consumed rapidly. When the separation distance increases from 11 mm to 24 mm, the maximum net reaction rate of CO increases and the corresponding axial distance increases gradually, which is consistent with the maximum net consumption rate of CH_4. When the separation distance is 11 mm, the maximum net reaction rate of CH_4 is small, resulting in the decrease of CO concentration. As a result, the concentration of CO involved in the oxidation reaction decreases and the maximum net consumption rate of CO is small. Accordingly, the concentration of CO_2 and H_2O decreases after the reduction of CO involved in the oxidation reaction. When the separation distance is 11 mm, the maximum net formation rate of CO_2 and H_2O is the minimum, as shown in Figs. 17a and 17b.

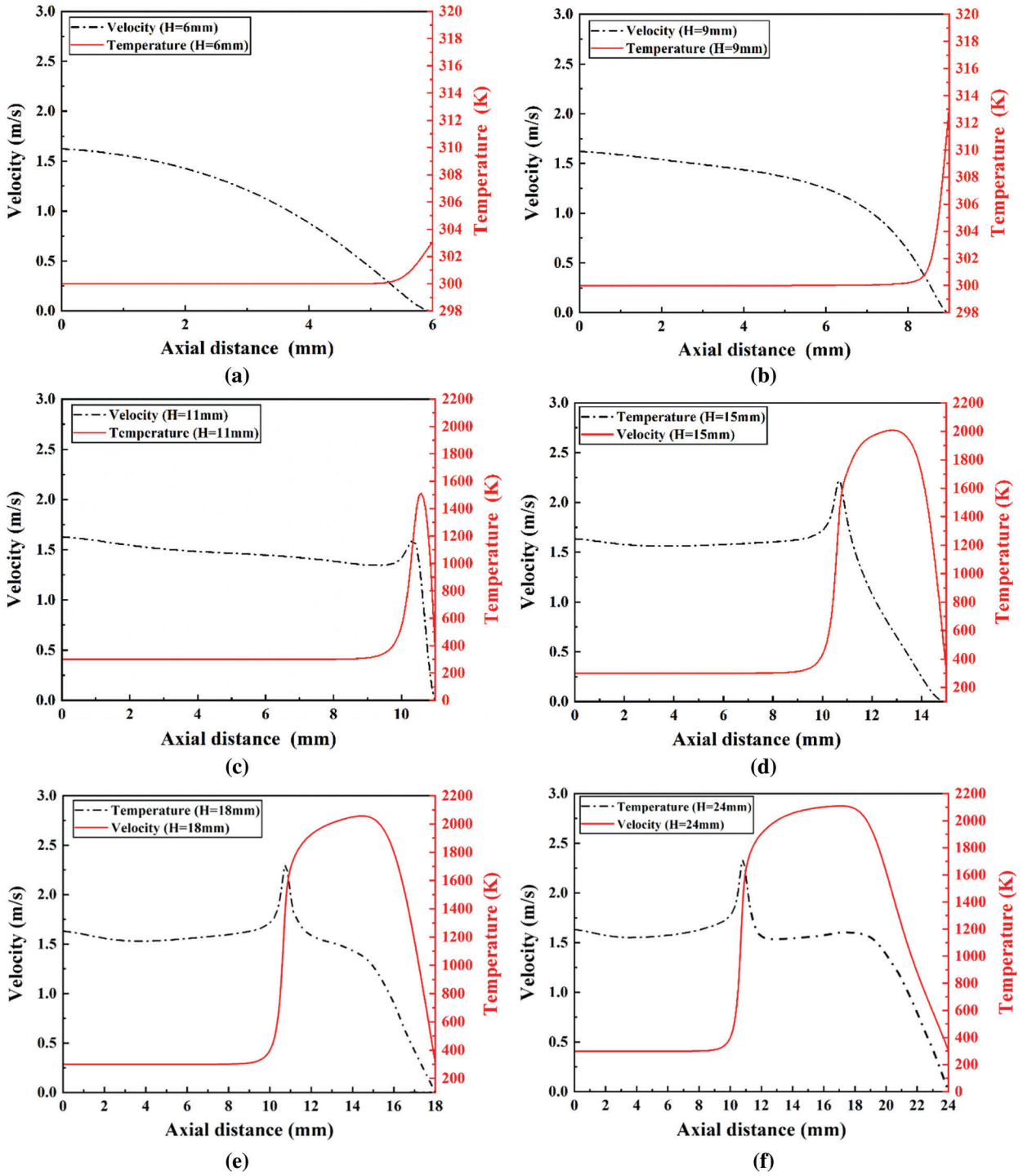

Figure 12: Temperature (solid line) and velocity (dotted line) distribution of mixture on the axis under different separation distances (a) separation distance of 6 mm (b) separation distance of 9 mm (c) separation distance of 11 mm (d) separation distance of 15 mm (E) separation distance of 18 mm (f) separation distance of 24 mm

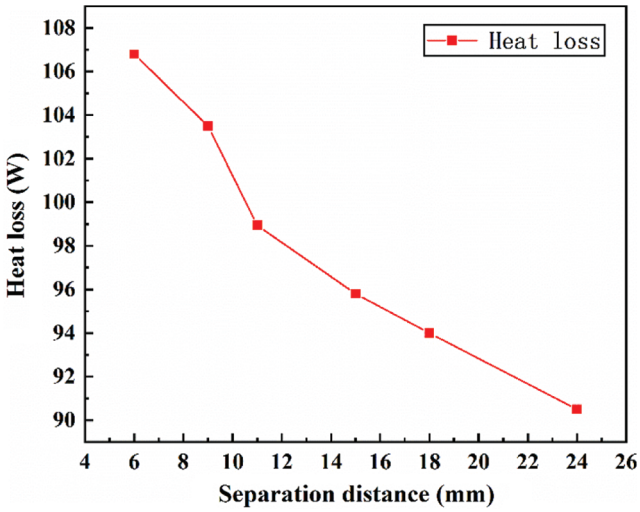

Figure 13: Wall heat loss under different separation distances

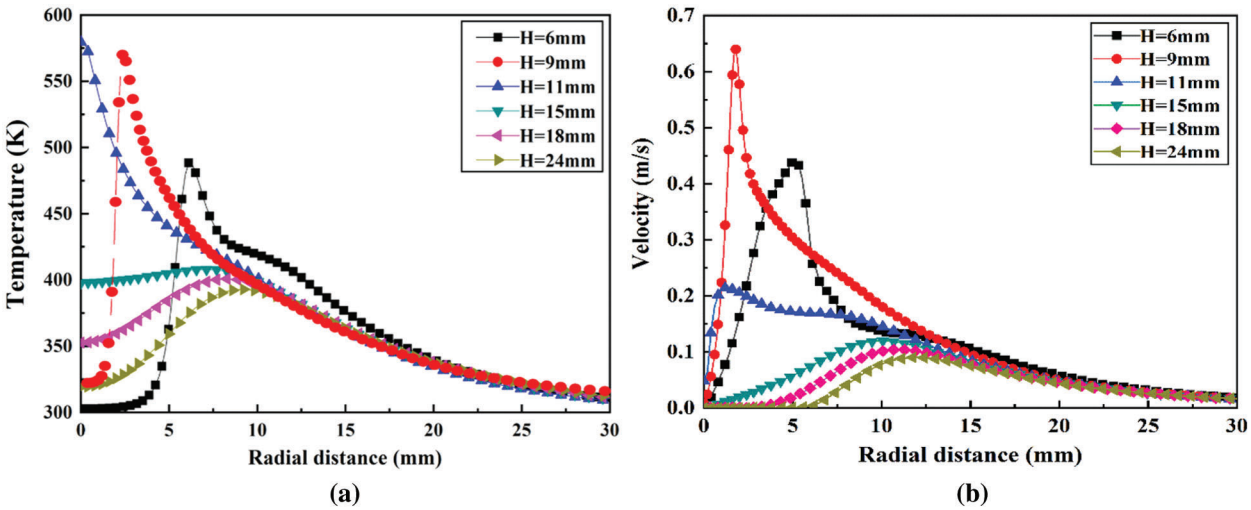

Figure 14: Temperature and velocity distribution in the radial direction near the wall (Z = 0.05 mm) at different separation distances (a) Temperature in radial direction near wall (b) Radial velocity near wall

3.4 Chemical Reaction Process Near the Wall

During the flame-wall interaction process, important chemical reactions occur near the wall, including the oxidation/decomposition reaction of CH_4/CH_3 (R57, R92), the decomposition reaction of HCHO (R50, R52) and CO formation/oxidation reaction (R20, R31, R34). Fig. 18 is a comparison diagram of the reaction rates of the above seven elemental reactions at the near – wall surface Z = 0.05 mm, and the separation distance H is 9 mm, 11 mm, and 18 mm.

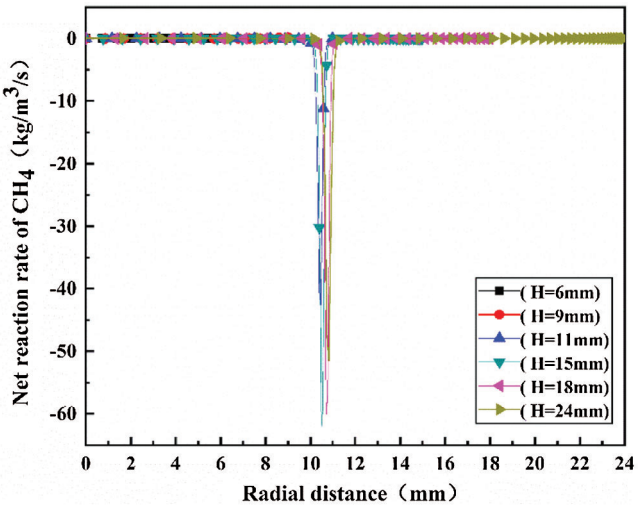

Figure 15: Effect of different separation distances on the net reaction rate of CH_4 on the symmetry axis

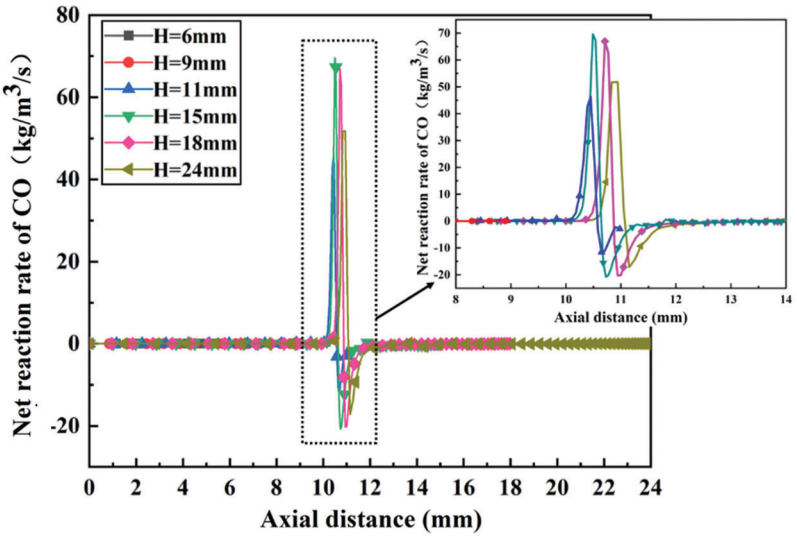

Figure 16: Effect of different separation distances on the net reaction rate of CO on the axis

It can be seen from the figure that as the separation distance increases, the reaction rates of the seven elementary elements gradually decrease. When H = 9 mm, the reaction rates of these seven elementary reactions are the highest. This indicates that when the separation distance is less than the height of premixed cone, the concentration of reactants near the wall is larger than that of other separation distances. It can be seen from Fig. 18 that when the separation distance is 9 mm, the peak points of the seven reaction rates all occur at a radial distance of 2.8 mm. When the separation distance increases to 11 mm, the tip of the premixing cone is closest to the stagnation point of the wall center. The mixture quickly comes into contact with the stagnation point of the wall after the reaction at the tip of the premixing cone is completed. Therefore, the chemical reaction is strongest at the center of the wall, and the peak of the reaction rate occurs at the stagnation point. As the radial distance increases, the reaction rate decreases rapidly. When the separation distance increases to 18 mm, the distance between the premixing cone and the wall is farther. Before reaching the wall, the premixed gas has already reacted

violently at the tip of the premixing cone, consuming a large amount of methane, resulting in fewer reactants near the wall. Therefore, when the separation distance is far, the reaction near the wall is weakened. The reaction rate is low, almost close to 0 kgmol/m^3/s. The peak position is also far from the stagnation point, occurring at a radial distance of 8 mm.

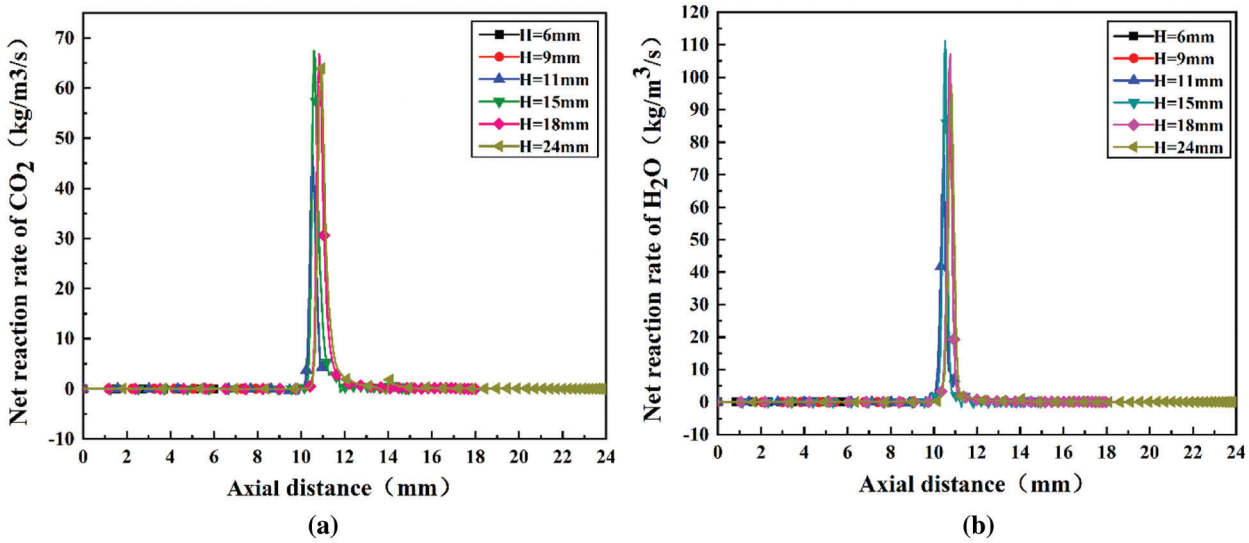

Figure 17: The effect of different separation distances on the net reaction rate of CO_2 and H_2O on the symmetry axis (a) Distribution of net CO_2 reaction rate on the axis (b) Distribution of net H_2O reaction rate on the axis

In addition, it can be seen from Fig. 18a that the rate of CH_4 oxidation reaction (R92) near the wall at H = 9 mm is greater than that of CH_3 decomposition reaction (R57). However, when H = 11 mm and 18 mm, the rate of CH_3 decomposition reaction (R57) is greater than that of CH_4 oxidation reaction (R92). This is because when the separation distance is greater than the premix cone (H = 11 mm and 18 mm), CH_4 has already undergone a strong chemical reaction at the tip of the premix cone before reaching the wall, and CH_3 is generated. Therefore, when the CH_4 concentration near the wall is reduced, the CH_3 concentration is higher, and the separation distance is smaller than the tip of the premixing cone. The chemical reaction mainly starts near the wall. It can be seen from Fig. 18c that the rate of CO oxidation (R20) at the three separation distances is higher than the rate of CO generation (R31, R34), which indicates that more CO_2 is generated near the wall. Moreover, the rate of CO generation/oxidation reaction at H = 9 mm is significantly higher than the reaction rate at H = 11 mm and 18 mm.

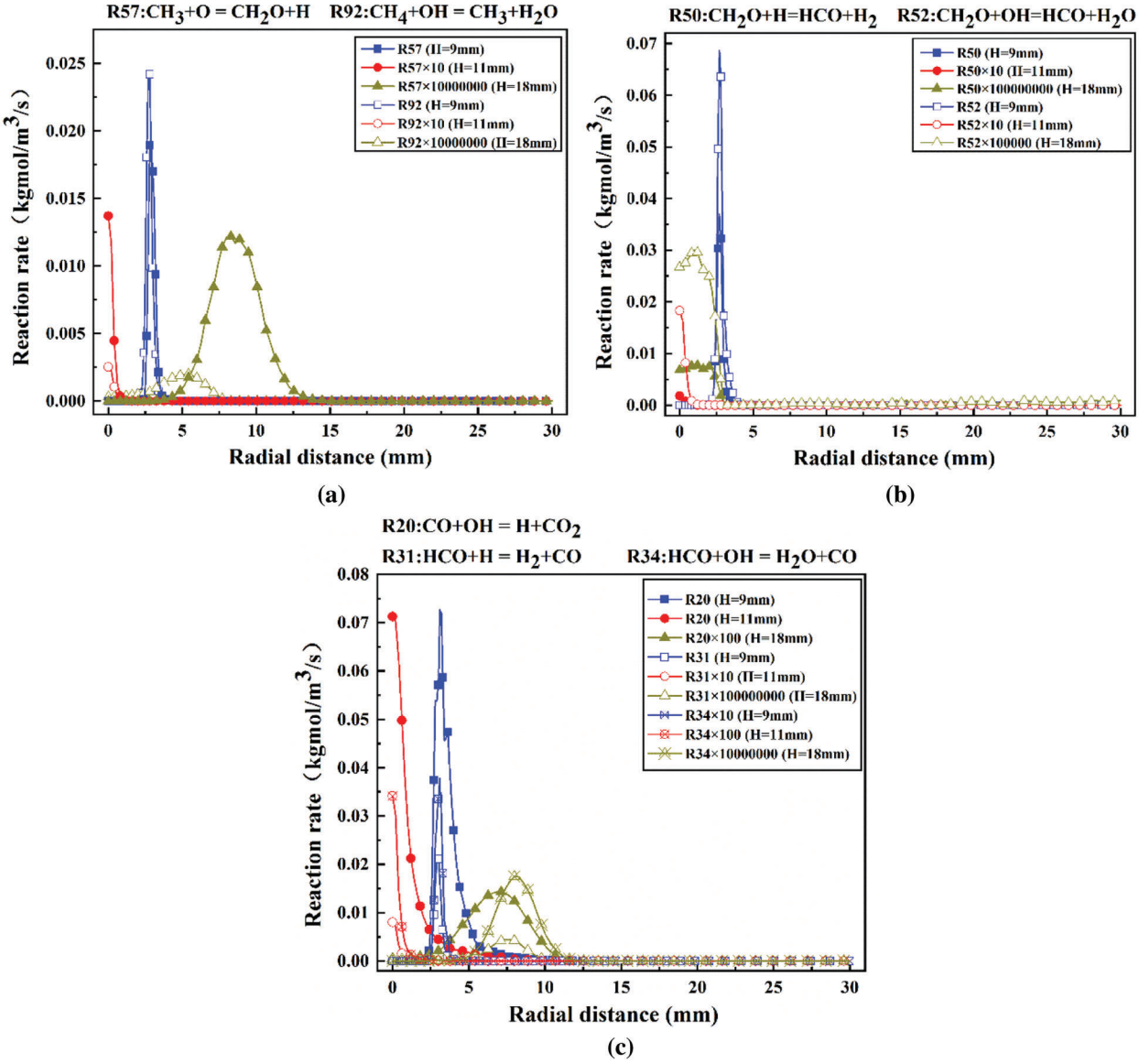

Figure 18: Main elementary reaction rates at different separation distances near the wall (a) CH_4/CH_3 oxidation/decomposition reaction (b) HCHO decomposition reaction (c) CO formation/oxidation reaction

4 Conclusion

This paper analyzes the combustion characteristics of CH_4/Air premixed jet flames at different separation distances. The effect of different separation distances on the flame shape of the premixed jet is mainly studied experimentally. And through the simulation method, the temperature and velocity distribution of the mixture at different separation distances, the reaction rate of key components, and the chemical reaction process near the wall are studied. The main conclusions are as follows:

(1) As the separation distance increases, the flame shape gradually becomes more complete from the trumpet shape. The height of the premix cone gradually increases, and then decreases gradually. When the separation distance is less than the height of the premix cone, a central cooling area parallel to the wall (cooling central core) will be formed. As the separation distance increases, the cooling center core

range gradually decreases until the separation distance is greater than the height of the premix cone and disappears. The concentration of CH gradually increases as the separation distance decreases, and it is the highest when the separation distance is 6 mm.

(2) As the separation distance increases, the temperature and velocity peaks on the axis will increase gradually. In the radial direction of Z = 0.05 mm near the wall, as the separation distance increases, the peak values of temperature and velocity of mixture first increase and then decrease. When the separation distance is 11 mm, the radial mixing temperature peak, velocity and temperature gradient are the largest.

(3) When the separation distance is less than the height of premixed cone, there is no reaction on the axis. When the separation distance is larger than the height of premixed cone, the peak value of net reaction rate and the corresponding axial distances of reactant (CH_4), intermediate (CO) and product (CO_2/H_2O) on the axis increase gradually with the increase of the separation distance and then decreases. And when the separation distance is 11 mm, the net reaction rate of CH_4 and CO is the smallest.

(4) The chemical reaction rate near the wall is related to the height of the premix cone and the separation distance. When the separation distance H = 9 mm, the chemical reaction near the wall is the maximum, and the peak point of the reaction rate occurs at the radial distance R = 2.8 mm. As the separation distance increases, the reaction rate gradually decreases, and the peak point of the reaction rate first moves to the stagnation point, and then moves in the radially increasing direction. And when H = 11 mm and 18 mm, because CH_4 undergoes a violent chemical reaction at the tip of the premixing cone and generates CH_3, the rate of the decomposition reaction of CH_3 (R57) is greater than that of the oxidation reaction of CH_4 (R92).

Funding Statement: This work was supported by the National Natural Science Foundation of China (Grant No. 51976082) and Qing Lan project.

Conflicts of Interest: The authors declare that they have no conflicts of interest to report regarding the present study.

References

1. Jainski, C., Rissmann, M., Boehm, B., Janicka, J., Dreizler, A. (2017). Sidewall quenching of atmospheric laminar premixed flames studied by laser-based diagnostics. *Combustion and Flame, 183,* 271–282. DOI 10.1016/j.combustflame.2017.05.020.
2. Gumus, M. (2009). Reducing cold-start emission from internal combustion engines by means of thermal energy storage system. *Applied Thermal Engineering, 29(4),* 652–660. DOI 10.1016/j.applthermaleng.2008.03.044.
3. Roberts, A., Brooks, R., Shipway, P. (2014). Internal combustion engine cold-start efficiency: A review of the problem, causes and potential solutions. *Energy Conversion and Management, 82,* 327–350. DOI 10.1016/j.enconman.2014.03.002.
4. Jainski, C., Martin, R., Mann, M., Dreizler, A. (2016). Flame-flow interaction in premixed turbulent flames during transient head-on quenching. *Flow Turbulence & Combustion, 98(4),* 1–14.
5. Frank, W., Alberto, B. (2011). A new method to warm up lubricating oil to improve the fuel efficiency during cold start. *SAE International Journal of Engines, 4(1),* 175–187. DOI 10.4271/2011-01-0318.
6. Andrae, J., BjöRnbom, P., Edsberg, L. (2002). Numerical studies of wall effects with laminar methane flames. *Proceedings of the Combustion Institute, 128(1–2),* 165–180.
7. Boust, B., Sotton, J., Labuda, S. A., Bellenoue, M. (2007). A thermal formulation for single-wall quenching of transient laminar flames. *Combustion and Flame, 149(3),* 286–294. DOI 10.1016/j.combustflame.2006.12.019.
8. Dreizler, A., BöHm, B. (2015). Advanced laser diagnostics for an improved understanding of premixed flame-wall interactions. *Proceedings of the Combustion Institute, 35(1),* 37–64. DOI 10.1016/j.proci.2014.08.014.
9. Bohlin, A., Mann, M., Patterson, B. D., Dreizler, A., Kliewer, C. J. (2015). Development of two-beam femtosecond/picosecond one-dimensional rotational coherent anti-stokes raman spectroscopy: Time-resolved

probing of flame wall interactions. *Proceedings of the Combustion Institute, 35(3),* 3723–3730. DOI 10.1016/j.proci.2014.05.124.

10. Drake, M. C., Haworth, D. C. (2007). Advanced gasoline engine development using optical diagnostics and numerical modeling. *Proceedings of the Combustion Institute, 31(1),* 99–124. DOI 10.1016/j.proci.2006.08.120.
11. Malikov, G. K., Lobanov, D. L., Malikov, K. Y., Lisienko, V. G., Viskanta, R. et al. (2001). Direct flame impingement heating for rapid thermal materials processing. *International Journal of Heat & Mass Transfer, 44(9),* 1751–1758. DOI 10.1016/S0017-9310(00)00204-0.
12. Kohse-HöInghaus, K., Barlow, R. S., Marcus, A., Jürgen, W. (2005). Combustion at the focus: Laser diagnostics and control. *Proceedings of the Combustion Institute, 30(1),* 89–123. DOI 10.1016/j.proci.2004.08.274.
13. Okkerse, M., Kleijn, C. R., Van Den Akker, H. E. A., De Croon, M. H. J. M., Marin, G. B. (2000). Two-dimensional simulation of an oxy-acetylene torch diamond reactor with a detailed gas-phase and surface mechanism. *Journal of Applied Physics, 88(7),* 4417–4428. DOI 10.1063/1.1309052.
14. Owston, R., Magi, V., Abraham, J. (2007). A numerical study of thermal and chemical effects in interactions of n-heptane flames with a single surface. *Combustion & Flame, 148(3),* 127–147.
15. Hindasageri, V., Vedula, R. P., Prabhu, S. V. (2014). Heat transfer distribution for impinging methane–air premixed flame jets. *Applied Thermal Engineering, 73(1),* 461–473. DOI 10.1016/j.applthermaleng.2014.08.002.
16. Ray, A., Chander, S. (2008). Heat transfer characteristics of laminar methane/air flame impinging normal to a cylindrical surface. *Experimental Thermal and Fluid Science, 32(2),* 707–721.
17. Jarray, M., Chetehouna, K., Gascoin, N., Bey, F. (2016). Ceramic panel heating under impinging methane-air premixed flame jets. *International Journal of Thermal Sciences, 107,* 184–195. DOI 10.1016/j.ijthermalsci.2016.04.014.
18. Tuttle, S. G., Webb, B. W., Mcquay, M. Q. (2005). Convective heat transfer from a partially premixed impinging flame jet. Part I: Time-averaged results-sciencedirect. *International Journal of Heat and Mass Transfer, 48(7),* 1236–1251. DOI 10.1016/j.ijheatmasstransfer.2004.10.027.
19. Tuttle, S. G., Webb, B. W., Mcquay, M. Q. (2005). Convective heat transfer from a partially premixed impinging flame jet. Part II: Time-resolved results. *International Journal of Heat and Mass Transfer, 48(7),* 1252–1266. DOI 10.1016/j.ijheatmasstransfer.2004.10.028.
20. Dabireau, F., Cuenot, B., Vermorel, O., Poinsot, T. (2003). Interaction of flames of H_2 + O_2 with inert walls. *Combustion and Flame, 135(1–2),* 123–133. DOI 10.1016/S0010-2180(03)00154-8.
21. Mann, M., Jainski, C., Euler, M., Bohm, B., Dreizler, A. (2014). Transient flame–wall interactions: Experimental analysis using spectroscopic temperature and CO concentration measurements. *Combustion and Flame, 161(9),* 2371–2386. DOI 10.1016/j.combustflame.2014.02.008.
22. Heinrich, A., Ganter, S., Kuenne, G., Jainski, C., Dreizler, A. et al. (2018). 3D numerical simulation of a laminar experimental SWQ burner with tabulated chemistry. *Flow, Turbulence and Combustion, 100(2),* 535–559. DOI 10.1007/s10494-017-9851-9.
23. Ganter, S., Heinrich, A., Meier, T., Kuenne, G., Jainski, C. et al. (2017). Numerical analysis of laminar methane–air side-wall-quenching. *Combustion and Flame, 186,* 299–310. DOI 10.1016/j.combustflame.2017.08.017.
24. Dong, L. L., Cheung, C. S., Leung, C. W. (2013). Characterization of impingement region from an impinging inverse diffusion flame jet. *International Journal of Heat and Mass Transfer, 56(1–2),* 360–369. DOI 10.1016/j.ijheatmasstransfer.2012.08.064.
25. Zhen, H. S., Leung, C. W., Cheung, C. S. (2011). Emission of impinging swirling and non-swirling inverse diffusion flames. *Applied Energy, 88(5),* 1629–1634. DOI 10.1016/j.apenergy.2010.11.036.
26. Dalvi, S., Karaliolios, E. C. J., Meer, T. H. V. D., Shahi, M. (2020). Thermo-magnetic convection in a circular annulus filled with magnetocaloric nanofluid. *International Communications in Heat and Mass Transfer, 116,* 104654. DOI 10.1016/j.icheatmasstransfer.2020.104654.
27. Titova, N. S., Kuleshov, P. S., Starik, A. M. (2011). Kinetic mechanism of propane ignition and combustion in air. *Combustion, Explosion, and Shock Waves, 47(3),* 249–264. DOI 10.1134/S0010508211030014.
28. Wang, F., Li, P., Mei, Z., Mi, J. (2013). Auto- and forced-ignition temperatures of diffusion flames obtained through the steady rans modeling. *Energy & Fuels, 28(1),* 666–677.

29. Höber, T., Suntz, R. (2018). Effect of different wall materials and thermal-barrier coatings on the flame-wall interaction of laminar premixed methane and propane flames. *International Journal of Heat and Fluid Flow, 69,* 95–105. DOI 10.1016/j.ijheatfluidflow.2017.12.004.

30. Zhao, D. Q., Yang, H. L., Wang, X. H. (2017). Combustion characteristics of non-premixed methane micro-jet flame in coflow air and thermal interaction between flame and micro tube. *Applied Thermal Engineering Design Processes Equipment Economics, 112,* 296–303.

31. Hou, S. S., Ko, Y. C. (2005). Influence of oblique angle and heating height on flame structure, temperature field and efficiency of an impinging laminar jet flame. *Energy Conversion and Management, 46(6),* 941–958. DOI 10.1016/j.enconman.2004.06.001.

32. Kuntikana, P., Prabhu, S. V. (2016). Heat transfer characteristics of premixed methane-air flame jet impinging obliquely onto a flat surface. *International Journal of Heat and Mass Transfer, 101,* 133–146. DOI 10.1016/j.ijheatmasstransfer.2016.05.004.

33. Chander, S., Ray, A. (2011). Experimental and numerical study on the occurrence of off-stagnation peak in heat flux for laminar methane/air flame impinging on a flat surface. *International Journal of Heat and Mass Transfer, 54(5–6),* 1179–1186. DOI 10.1016/j.ijheatmasstransfer.2010.10.035.

34. Bohlin, A., Jainski, C., Patterson, B. D., Dreizler, A., Kliewer, C. J. (2017). Multiparameter spatio-thermochemical probing of flame–wall interactions advanced with coherent raman imaging. *Proceedings of the Combustion Institute, 36(3),* 4557–4564.

35. Chander, S., Ray, A. (2006). Influence of burner geometry on heat transfer characteristics of methane/air flame impinging on flat surface. *Experimental Heat Transfer, 19(1),* 15–38. DOI 10.1080/08916150500317655.

36. Chander, S., Ray, A. (2007). Heat transfer characteristics of three interacting methane/air flame jets impinging on a flat surface. *International Journal of Heat and Mass Transfer, 50(3–4),* 640–653. DOI 10.1016/j.ijheatmasstransfer.2006.07.011.

37. Kleijn, C. R. (2000). Heat transfer from laminar impinging methane/air flames. *American Society of Mechanical Engineers, Pressure Vessels and Piping Division (Publication) PVP, 424,* 259–269.